

# Functionalization of 3D printed scaffolds using polydopamine and silver nanoparticles for bone-interfacing applications

Alessandra Merlo<sup>1</sup>, Eduardo Gonzalez-Martinez<sup>2</sup>, Kamal Saad<sup>3</sup>, Mellissa Gomez<sup>2</sup>, Manjot Grewal<sup>2</sup>, Joseph Deering<sup>1</sup>, Liza-Anastasia DiCecco<sup>1</sup>, Zeinab Hosseinidoust<sup>2,4,5</sup>, Kyla Sask<sup>1,4,5</sup>, Jose M. Moran-Mirabal\*<sup>2,4,5,6</sup>, Kathryn Grandfield\*<sup>1,4,5</sup>

<sup>1</sup> *Department of Materials Science and Engineering, McMaster University, Hamilton, ON, L8S 4L8, Canada*

<sup>2</sup> *Department of Chemistry and Chemical Biology, McMaster University, Hamilton, ON, L8S 4L8, Canada*

<sup>3</sup> *School of Interdisciplinary Science, McMaster University, Hamilton, ON, L8S 4L8, Canada*

<sup>4</sup> *School of Biomedical Engineering, McMaster University, Hamilton, ON, L8S 4L8, Canada*

<sup>5</sup> *Brockhouse Institute for Materials Research, McMaster University, Hamilton, ON, L8S 4L8, Canada*

<sup>6</sup> *Centre for Advanced Light Microscopy, McMaster University, Hamilton, ON, L8S 4L8, Canada*

Corresponding authors: Kathryn Grandfield ([kgrandfield@mcmaster.ca](mailto:kgrandfield@mcmaster.ca)), 1280 Main St W, Hamilton, ON L8S 4L8, Canada.

Jose M. Moran Mirabal ([mirabj@mcmaster.ca](mailto:mirabj@mcmaster.ca)) 1280 Main St W, Hamilton, ON L8S 4L8, Canada.

## 1. Abstract

The prevention of bacterial colonization and the stimulation of osseointegration are two major requirements for bone-interfacing materials to reduce the incidence of complications and promote the restoration of the patient's health. The present investigation developed an effective, two-step functionalization of 3D printed scaffolds intended for bone-interfacing applications using a simple polydopamine (PDA) dip-coating method followed by the formation of silver nanoparticles (AgNPs) after a second coating step in silver nitrate. 3D-printed polymeric substrates coated with a ~20 nm PDA layer and 70 nm diameter AgNPs proved effective in hindering *Staphylococcus aureus* biofilm formation, with a 3000-8000-fold reduction in the number of bacterial colonies formed. The implementation of both porous geometries significantly accelerated osteoblast-like cell growth. Microscopy characterization further elucidated homogeneity, features, and penetration of the coating inside the scaffold. A proof-of-concept coating on titanium substrates attests to the transferability of the method to other materials, broadening the range of applications both in and outside the medical sector. The antibacterial efficiency of the coating is likely to lead to a decrease in the number of bacterial infections developed after surgery in presence of these coatings on prosthetics, thus translating to a reduction in revision surgeries and improved health outcomes.

Keywords: antibacterial, coating, prosthetics, additive-manufacturing, biointerfaces

## 2. Introduction

The success of synthetic biomaterials as bone-interfacing implants to replace or restore functionality in patients is, in part, determined by two factors: the prevention of bacterial infections, and favorable interaction between the material and the bone through the process of osseointegration<sup>1</sup>. Infections are the result of bacterial contamination of the implant surface with subsequent production of extracellular polysaccharides and the formation of a bacterial biofilm<sup>2</sup>. Antibiotics are commonly prescribed for surgeries to prevent or limit bacterial infections<sup>3</sup>, but are reportedly less effective in killing bacteria once a biofilm is formed. Diminished effectiveness of the antibiotics is due to limited penetration of the antibiotic in the biofilm, or to bacterial adaptive stress responses<sup>4,5</sup>. Therefore, the prevention of biofilm formation on biomaterials is an important topic in biomedical research, with various methods being reported over the years to achieve antimicrobial surfaces<sup>6,7</sup>. A large portion of these methods focuses on the introduction of surface functionalization, with a diverse range of techniques and surface chemistries, to reduce bacterial adhesion and subsequent biofilm formation. In this context, dopamine has emerged as a simple, versatile and effective biocompatible surface coating with outstanding adhesive properties on different materials<sup>8</sup>. Under alkaline conditions (pH > 8.0), dopamine undergoes a spontaneous oxidative polymerization in solution to form a layer of polydopamine (PDA) on substrates, relying on different bonding mechanisms (*e.g.*, pi-pi stacking, hydrogen bond formation, and/or covalent bonding) depending on the surface chemistry of the target substrate<sup>8</sup>. The broad range of organic and inorganic substrates to which the compound can bind<sup>8</sup> and the multiple organic moieties exposed to the media in the PDA layer that are readily available for further chemical modifications<sup>9–12</sup> have made PDA a versatile and effective surface functionalization method for use in diverse applications, including rechargeable batteries<sup>13</sup>, sensors<sup>14</sup>, water treatment membranes<sup>15</sup>, antifouling surfaces<sup>16</sup>, biomedical devices<sup>17</sup>, catalytic materials<sup>18</sup>, among others<sup>19</sup>. The characteristics of dopamine layers, including homogeneity and thickness, depend on a number of variables, like the duration of the contact between the dopamine solution and the substrate, the surface chemistry of the substrate or the temperature of the reaction<sup>20–23</sup>. PDA coating of a substrate constitutes an effective surface preparation technique for the subsequent immobilization or nucleation of various metal nanoparticles<sup>9,24–26</sup>. In this sense, silver nanoparticles (AgNPs) have often been suggested for antimicrobial applications given their antibacterial properties<sup>27,28</sup>. Although such characteristic was often assumed to be linked to cytotoxicity and genotoxicity toward mammalian cells<sup>29</sup>, it is dependent on the nanoparticle size<sup>29–31</sup>, concentration<sup>32</sup>, and the specific cell line<sup>33</sup>.

Proper osseointegration is also crucial in determining the applicability of a biomaterial *in vivo*. Porous structures, when specifically engineered for pore size, interconnectivity, and mechanical properties, can favor osseointegration by promoting cell infiltration and proliferation, and the formation of early vasculature<sup>34–38</sup>. While porous substrates favor bone ingrowth and secondary stability of a prosthesis, the application of homogenous coatings inside porous structures is not a trivial matter. In this study, a two-stage surface modification method was used to produce antibacterial properties on porous substrates, while maintaining cytocompatibility with osteoblast-like cells. The PDA coating was synthesized on 3D printed porous polymeric substrates as an adhesion layer that allowed the nucleation of AgNPs on the surface. The efficacy of the functionalization was probed through bacterial testing with *Staphylococcus aureus*, both in the planktonic state and for the prevention of biofilm formation. Surface coverage of the internal porous network with the engineered coating was evaluated to assess the penetration of the coating in the internal sections of the scaffolds. A proof-of-concept experiment for implants was conducted using titanium scaffolds and confirmed the transferability of the method to different types of materials, attesting to its wide applicability.

## 3. Materials and Methods

### 3.1 Materials

Silver nitrate ( $\text{AgNO}_3$ , 99.999%), hydrochloric acid (HCl) and dopamine hydrochloride (DA) were purchased from Sigma-Aldrich (Oakville, ON, Canada). Ethanol, acetone, and isopropanol (IPA, 99.5 %) were acquired from Fisher Scientific (Ottawa, ON, Canada). Vinyl adhesive tape (FDC-4300) was purchased from FDC Graphic Films (South Bend, IN, USA). Polymeric substrates were manufactured using UV-sensitive resin purchased from Anycubic© (Shenzhen, China). Carbon tape was purchased from Ted Pella Inc. (Redding, CA, USA). Tryptic soy broth (TSB) (211825), agar (BP1423-500), and phosphate buffered saline (PBS) (BP2944-100) were purchased from Fisher Scientific (Ottawa, ON, Canada). TSB was prepared to 3% in deionized water and PBS was prepared as per manufacturer's instructions. TSB plates were prepared using a 3% TSB and 1.5% agar solution. Milli-Q water with a resistivity of 18.2 M $\Omega$  cm (Milli-Q Advantage A10 Water Purification system, Millipore Sigma, Etobicoke, Canada) was used for all synthesis steps.

### 3.2 3D Printing of Scaffolds

Polymeric substrates were manufactured by 3D-printing using an Anycubic© 3D printing UV-sensitive polyurethane acrylate-based resin and an Anycubic© Photon S printer using a 405 nm wavelength. Solid and porous cylindrical substrates were printed with equal dimensions, 13 mm diameter and 3 mm thickness, but with the porous substrate having 1000  $\mu\text{m}$  homogeneous porosity. Both structures were designed on Anycubic© Photon Slicer software. After manufacturing, the substrates were rinsed in an ethanol bath and subjected to a post-printing UV-crosslinking finishing step using a UVP TL-2000 Ultraviolet Translinker. Prior to coating, all resin substrates were rinsed in two steps, first in isopropanol and then in Milli-Q water, nitrogen dried, and then air plasma-treated for 5 minutes using a PDC expanded plasma cleaner (Harrick, Ithaca, NY, USA) at high power (30 W) and directly used for the first functionalization step.

### 3.3 PDA coating and AgNP deposition

Following the procedure described in <sup>14</sup> by Gonzalez et al., the PDA coating was applied by dip-coating the substrate in a 2 mg/mL solution of dopamine hydrochloride in Tris-Buffer (pH 8.5) for 24 hours. Prior to the second functionalization step, samples were water rinsed and nitrogen dried. AgNPs were subsequently nucleated through dip-coating: the substrates were immersed in a 0.1 M solution of silver nitrate ( $\text{AgNO}_3$ ) in Milli-Q water, then incubated at room temperature on an orbital shaker (90 rpm) for 24 hours. Following nucleation, the substrates were washed with Milli-Q water, and nitrogen dried.

Silicon wafers were coated in the same way to evaluate the PDA layer thickness. Silicon wafers for coating thickness measurement, purchased from University Wafer Inc. (FL, USA), were cleaved into 1.5 x 0.5 cm pieces with a diamond tip pen. Half of the wafer piece was masked with adhesive tape prior to PDA layer formation via dip-coating approach, following the protocol described for resin substrates. Once the polymerization time had elapsed the adhesive tape was removed, leaving one half of the substrate coated with a PDA layer and the other side bare for use as a baseline comparison for thickness calculation.

A tape test was conducted to assess the adhesion strength of the coatings to the substrates using Elcometer® 99 Adhesive Tape (ASTM D3359-17). For such tests, the PDA coating was applied on the solid scaffolds by dip-coating the substrates in a 2 mg/mL solution of dopamine hydrochloride for 24 hours. The substrates were then washed, dried and submerged into a 0.1 M solution of  $\text{AgNO}_3$  for 24 hours for the deposition of nanoparticles, as more thoroughly described in the previous section. A low-adhesion negative control was prepared by drop casting technique to deposit a PDA coating on the same 3D printed substrates, and subsequent electroless deposition of copper from solution, as more thoroughly described in the work by Gonzalez et al <sup>14</sup>. On all substrates tape was applied and peeled off. Images of the substrate before test, and of the tape and substrate after test, were captured using a phone camera.

### 3.4 Microscopy characterization

The thickness of the PDA coating was measured and averaged over 3 independently prepared samples using an MFP-3D (Asylum Research, CA, USA) Atomic Force Microscope (AFM) in AC mode. Two measurements over an area of 12x12  $\mu\text{m}$  were recorded for each sample. The thickness was evaluated as the difference

between coated and non-coated silicon substrate profiles using Gwyddion 2.55 software. To characterize the surface for coverage and size of nanoparticles, an FEI Magellan 400 (Thermo Fisher; Waltham, MA, USA) was used to perform scanning electron microscopy (SEM) analysis with an accelerating voltage of 2 kV for secondary electron imaging. All resin samples for electron microscopy were sputter-coated before imaging using the Precision Etching and Coating System (PECS) (Gatan Inc.; Warrendale, PA, USA) with 5 nm of platinum. ImageJ software<sup>39</sup> was used for image analysis. To exclude any aggregates and outliers from the measurements, a range of 500 – 55000 nm<sup>2</sup> for particle area was selected as a threshold. Three images were analyzed for each of the substrates.

### 3.5 Depth of penetration of the PDA coating

To gather a qualitative understanding of the coating penetration in porous scaffolds, two scenarios were considered, inspired by the work of Deering et al.<sup>40</sup>, either prior to the PDA coating step or before the nucleation step described above, as depicted in Figure 1. In the first case, referred to as Scenario 1, the bottom and top surfaces were covered with carbon tape after the PDA functionalization step, so that the perfusion of the silver nitrate solution was limited to the radial direction. In the second case, referred to as Scenario 2, both the bottom and top circular surfaces were coated with carbon tape at the beginning of the process, so that the perfusion was exclusive to the radial direction in both steps of the functionalization. All parameters of the functionalization were maintained equal to what was previously described.

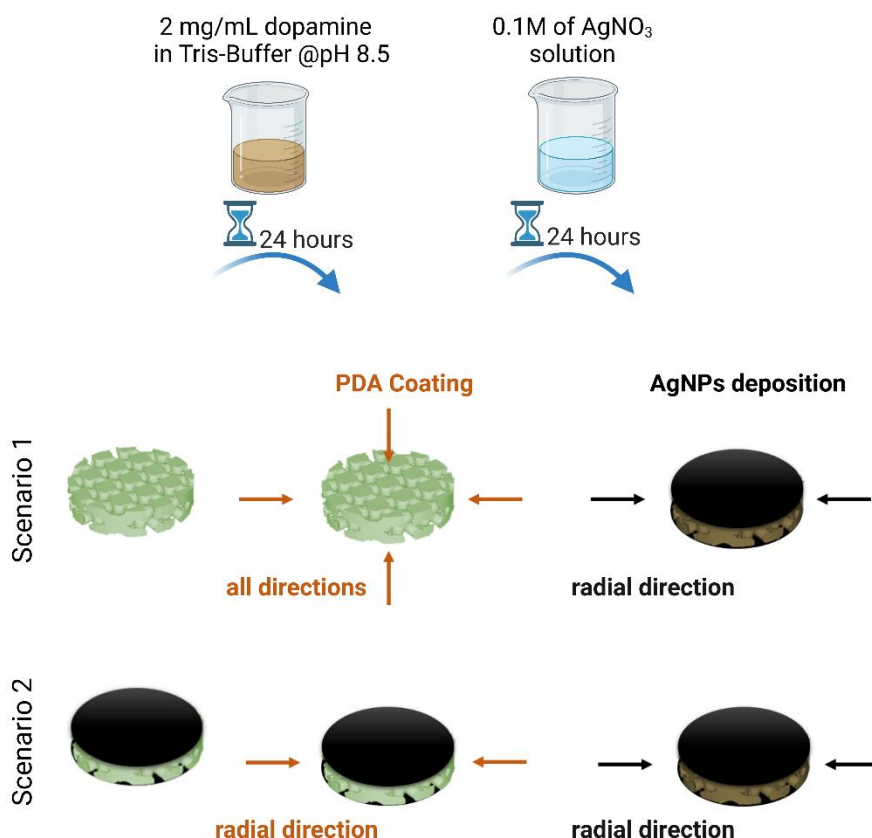


Figure 1. Schematic depicting the carbon tape coating process to evaluate the depth of penetration of the two-step functionalization. Black arrows indicate directions of infiltration of the polydopamine/silver nitrate solutions. Created with BioRender.

### 3.6 Cell culture and metabolism

Saos-2 osteosarcoma cells (ATCC®, HTB-85) were grown in McCoy's 5A modified medium (Life Technologies Inc.; Carlsbad, CA, USA) with 13% fetal bovine serum (Life Technologies Inc; Carlsbad, CA, USA) and 1% penicillin/streptomycin (Sigma-Aldrich; Oakville, ON, Canada). Six samples of each condition were rinsed with ethanol and nitrogen dried, and then sterilized with 10 min exposure to UV light on both the top and bottom

circular surfaces. Cells were seeded at a density of  $10^4$  cells/cm<sup>2</sup> and incubated at 37 °C with 5% CO<sub>2</sub>, and culture media exchanged every two days. Cell metabolism was assessed with an AlamarBlue<sup>®</sup> assay (Life Technologies Inc., Carlsbad, CA, USA) on days 1, 4 and 7. An Infinite M200 Pro plate reader (Tecan Group Ltd., Switzerland) was used to measure the fluorescence intensity values at 540 nm excitation and 580 nm emission wavelengths. Statistical differences were measured using a two-way ANOVA with Tukey's HSD test in GraphPad Prism software (San Diego, CA, USA). The significance level was defined at 0.05.

### 3.7 *In vitro* quantification of antimicrobial activity

Antimicrobial activity was tested against *Staphylococcus aureus* strain Newman, a strain that was isolated from a human infection<sup>41</sup>. *S. aureus* overnight cultures were inoculated in TSB media and grown for 18 hours at 37 °C within a shaking incubator. The polymer substrates were incubated in *S. aureus* bacterial suspensions to assess antimicrobial activity. All substrates were sterilized prior to experiments by rinsing with ethanol followed by drying with nitrogen gas. Substrates were then transferred to a biological safety cabinet and UV sterilized for ten minutes on both the top and bottom circular surfaces. Analysis of biofilm formation was completed using a similar method performed by Kucharíková et al.<sup>42</sup>. The substrates were placed into a 24-well flat bottom plate (10861-558; VWR, Mississauga, ON, Canada) followed by 1 mL of *S. aureus* suspensions at a concentration of  $1.6 \times 10^4$ ,  $8.5 \times 10^4$ , and  $7.3 \times 10^5$  CFU/ml to prepare biological triplicate measurements. The enclosed well plate was incubated for 24 hours at 37 °C with an open reservoir of saturated salt solution. The saturated salt solution provided a humidified environment<sup>43</sup>, thus minimizing suspension evaporation. Substrates were washed with 2 mL of PBS to remove non-adherent bacteria. The substrates were then individually transferred into sterile falcon tubes containing 2 mL of PBS, sonicated for 10 minutes, and vortexed for 1 minute to dislodge the adherent bacteria. The samples were then serially diluted in PBS and plated on TSB agar plates in duplicate. Plates were incubated at 37 °C for 24 hours prior to enumeration. Biofilm concentration was quantified in terms of the number of colony-forming units (CFU) per mL produced from the dislodged bacteria.

The effect of the substrate on the surrounding *S. aureus* bacterial suspension was assessed by measuring the opacity of the suspension after 24 hours of incubation. The optical density of a bacterial suspension can be correlated to its concentration. The sterilized substrates were individually placed into the wells of a 24-well plate. Three overnight cultures of *S. aureus* were diluted in TSB to a relatively low concentration of  $1.6 \times 10^4$ ,  $8.5 \times 10^4$ , and  $7.3 \times 10^5$  CFU/mL. 1 mL of each culture was then added to the substrate-containing wells in biological triplicate experiments. As a control, three wells were filled with 0.6 mL of  $5.25 \times 10^4$  CFU/mL *S. aureus* each, and three additional wells were filled with 1 mL of TSB media each. The enclosed well plate, along with an open reservoir of saturated salt solution, was placed in a 37 °C static incubator for 24 hours. Following incubation, the substrates were removed from the wells and the opacity of the remaining suspension was measured using a plate reader (Synergy Neo2; Agilent, Mississauga, ON, Canada). Optical density (OD) of the remaining *S. aureus* bacterial suspension was measured at 600 nm and corrected for the optical density of the TSB media. Statistically significant differences on the log-transformed data were determined using a two-way ANOVA (GraphPad Software, San Diego, CA, USA).

### 3.8 *Inductively coupled plasma–optical emission spectroscopy (ICP-OES) analysis*

ICP-OES was used to evaluate the leaching of silver ions from the substrates into solution. Solid and porous substrates with PDA coating and AgNPs, in triplicates, were incubated in 1 mL TSB at 37 °C for 24 hours, as done for the bacterial testing. Milli-Q water was used for all sample and calibrant dilutions. At 24 hours, the 1 mL TSB solutions were collected, adjusted to a pH value of 5 using 20 µL of 0.5 M HCl to prevent silver ion precipitation, and filled to 5 mL using Milli-Q water followed by vortexing. A 6 ppm Ag<sup>+</sup> stock was prepared by serially diluting a 1000 ppm Ag<sup>+</sup> stock. Calibration standards at 0, 0.01, 0.05, 0.1, 0.25, 0.5, 0.75 and 1 ppm Ag<sup>+</sup> were prepared as 5 mL solutions using the 6 ppm Ag<sup>+</sup> stock, where the matrix consisted of 1 mL TSB and 20 µL 0.5 M HCl to mimic the samples, and was filled to 5 mL with Milli-Q followed by vortexing. Calibrants and samples were run using the Vista-PRO CCD Simultaneous ICP-OES (Varian, Mississauga, ON, Canada).

Emission intensities at 328, 338 and 241 nm were recorded by Varian's ICP Expert II system software. The emission intensity was highest at 328 nm, therefore a calibration curve was plotted using corrected emission intensity at 328 nm on Microsoft Excel (Microsoft Office, Redmond, WA, USA). Linear regression was used to determine the  $[Ag^+]$  in the TSB samples where the 5-fold dilution for the samples was accounted for during analysis, and the  $R^2$  value was calculated through the Microsoft Excel function.

### 3.9 Cytotoxicity of silver ions toward Saos-2 cells

In order to evaluate the cytotoxicity of silver ions in solution toward the cell line under investigation, a 2 g/mL stock solution of  $AgNO_3$  in Milli-Q water was prepared. The stock solution was then filtered through a 0.2  $\mu m$  filter unit to eliminate contaminants and impurities. Saos-2 osteosarcoma cells (ATCC<sup>®</sup>, HTB-85) were grown in the same conditions described in the paragraph above. Cells were seeded at a density of  $10^4$  cells/cm<sup>2</sup> and incubated at 37 °C with 5% CO<sub>2</sub>. For this purpose, the supplemented media was further supplemented with decreasing contents of the 2 g/mL silver nitrate solution, as similarly done by Hildago et al <sup>44</sup>, in order to obtain concentrations of silver ions equal to 10, 1, 0.1 and 0 ppm. After 24 hours, cells were stained using a LIVE/DEAD Cell Imaging Kit (Cat. # R37601, Invitrogen, Waltham, MA, US) following the directions of the manufacturer, and imaged using a Nikon A1 Inverted Confocal microscope. Results on viability were evaluated using ImageJ software on the captured images.

### 3.10 Proof-of-concept on titanium substrates

Titanium disks (d = 15 mm, h = 1.25 mm) were obtained by cutting Grade 2 unalloyed titanium sheets (ASTM-B-265-13A, McMaster-Carr). First, titanium squares (16 mm x 16 mm) were produced, then using lathe and blade, they were cut to produce the disks. Following manufacturing, all titanium substrates were rinsed in three steps, first in ethanol, then in acetone and then in Milli-Q water, and then nitrogen dried. All subsequent steps for functionalization were consistent with what described above.

## 4. Results and Discussion

In the present research, a two-step surface functionalization approach was investigated to promote preliminary cytocompatibility and prevent bacterial colonization. Both porous and solid substrates were considered, since porous scaffolds are known to promote preliminary osseointegration <sup>37</sup>. The first step of the functionalization technique consisted of the formation of a PDA layer on the substrate through dip-coating in a dopamine hydrochloride solution in Tris buffer (pH 8.5), where the dopamine spontaneously polymerized to coat the material. The thickness of the PDA coating on a substrate is dependent on different variables such as the solution pH, the PDA concentration, the temperature of the reaction, and the selected deposition time <sup>8</sup>. The synthesis parameters selected in the present work are optimized based on previous work from Gonzalez-Martinez et al. <sup>14</sup>, in order to obtain the thinnest and smoothest film that could produce a uniform AgNP deposition. The 24-hour dip-coating of silicon wafers in dopamine solution resulted in the deposition of polydopamine (PDA) coatings with a thickness of approximately 22 ( $\pm 3$ ) nm, as measured by atomic force microscopy analysis shown in Figure 2. The bright region in the center of the Figure 2a is likely due to solution pooling and aggregation of the PDA film at the boundary with the vinyl tape, which obscures a sharp edge.

The values measured in the current investigation agree with previous literature results <sup>8,14,19</sup>.

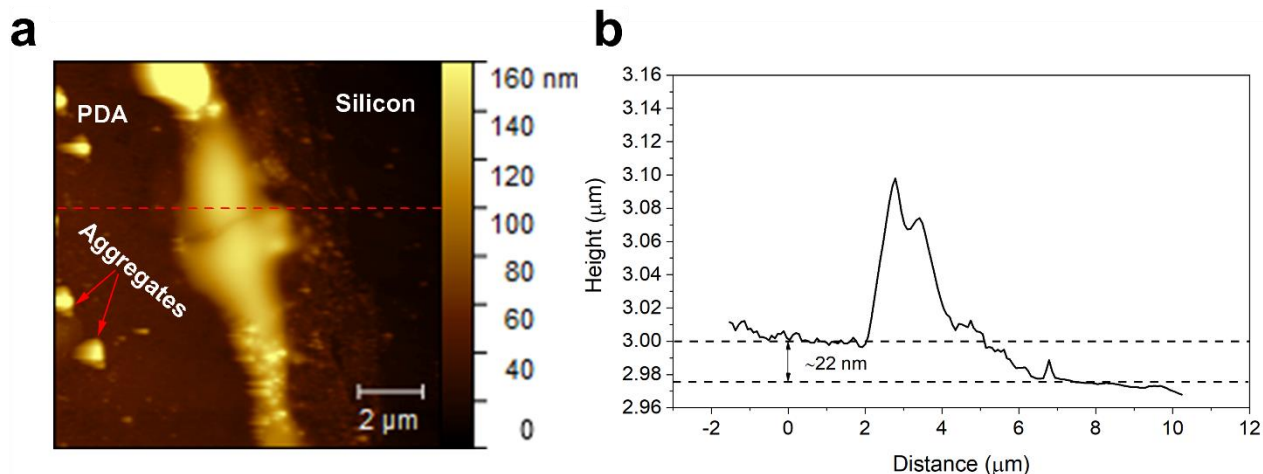


Figure 2. a) Representative AFM image showing the edge between the PDA coating covered with vinyl tape prior to the first functionalization step. PDA aggregates are indicated in the image by red arrows. The coating profile along the dotted red line is presented in b), from which the approximate coating thickness of the PDA is evaluated.

When submerged in a solution of silver nitrate, PDA acts as a reducing agent for silver ions ( $\text{Ag}^+$ ) to form the AgNPs. The deposition of AgNPs on PDA-coated surfaces was similarly demonstrated in an experiment conducted by Lu et al.<sup>45</sup>, where a layer of AgNPs was deposited on the surface of PDA-coated silk fibers to confer antibacterial functionality. The 3D printed scaffolds, functionalized in two steps as described above (Figure 1), were characterized for the surface coverage with AgNPs and the nanoparticle size. The nucleation of AgNPs on top of the PDA-coated substrates was qualitatively assessed through the appearance of a yellow, opaque tint on the substrate after nanoparticle deposition on the material's surface, as clearly visible on the borders of the porous substrate (Figure 2S). Such qualitative evaluation was confirmed by scanning electron microscopy (SEM) characterization (Figure 3).

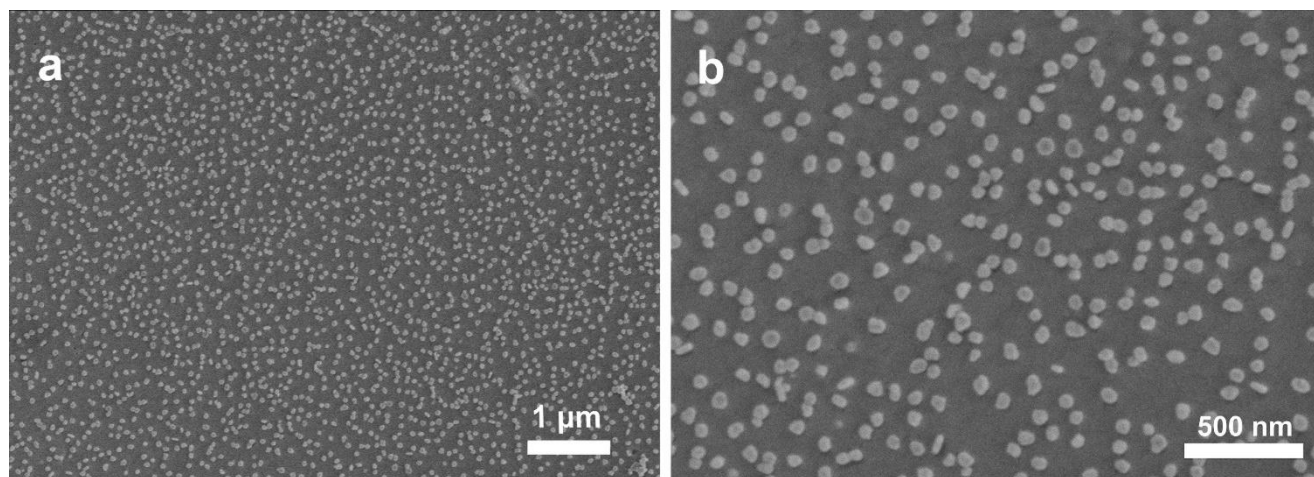


Figure 3. Overview (a) and magnified (b) SEM micrograph showing the surface coverage of a resin substrate functionalized with PDA coating and subsequent silver nanoparticle nucleation. Roughly 18% of the surface was covered in AgNPs with a diameter of  $71 \pm 4$  nm.

Image analysis of the micrographs was conducted with ImageJ software, using an area threshold to exclude aggregates, which would bias the average particle diameter evaluation. Results showed that the AgNPs were uniformly distributed over the surface of solid resin substrates. The percentage coverage of AgNPs over the solid surface was measured at  $18.3 \pm 0.5\%$ , with an average particle area equal to  $3900 \pm 300 \text{ nm}^2$ . The aspect ratio was close to one ( $1.3 \pm 0.3$ ) for AgNPs on resin substrates which indicates a nearly circular shape. Using the average particle area and assuming circular particles, the equivalent diameter of the particles on compact resin substrates was measured at  $71 \pm 4$  nm. An example of the image analysis procedure for nanoparticle

size evaluation is provided in Figure S3 of the Supporting information, complemented by a histogram showing the distribution of the nanoparticles sizes.

To assess the adhesion of the PDA layer to the polymeric substrate, a tape test was conducted. Four different substrates were tested: a bare 3D printed substrate, a substrate coated with a polydopamine layer, one with PDA coating and nucleated nanoparticles, both obtained following the protocol described, and finally a control prepared by PDA coating of the bare 3D printed substrates and subsequent electroless deposition of copper from solution. The latter would serve as a negative control, given the known poor adhesion copper presents toward the substrates under investigation. The results of such test are displayed in Figure S4 of the Supporting Information for publication: no noticeable difference is found in the behaviour of the bare and PDA-coated substrates. On the contrary, the silver nanoparticles partially detached from the layer of polydopamine after peeling. While the peel test is only partially representative of *in vivo* stress conditions, such findings suggest that further analysis on the use of this coating for areas which undergo tribological stresses are required, especially to address how silver nanoparticles would then interact within the body. However, such investigation is beyond the scope of the present work, and will be the subject of future research.

The homogeneous infiltration of both dopamine and silver nitrate solutions into complex geometries is a prerequisite to form these antibacterial coatings with complete coverage of an implant material. In the presence of multiscale topography, another common attribute of an implant surface that results in favorable osseointegration<sup>46,47</sup>, the precursor dopamine and silver solutions need direct exposure to these topographically complex areas to create functionalized surfaces. To obtain a qualitative understanding of the coating penetration, two scenarios were considered, as depicted in the scheme in Figure 1. One where the PDA coating step was completed normally and then carbon tape was applied on the top and bottom surfaces before the substrate was immersed in the silver nitrate solution (Scenario 1), and another where carbon tape was applied before the PDA coating step (Scenario 2).

When the carbon tape was applied following the first functionalization step, nanoparticle coverage of the substrate was observed both in the external (Figure 4, a-c) and internal (Figure 4 d-f) pores. Conversely, when the substrates were covered with carbon tape before the PDA functionalization step, AgNP coverage was observed on the external surfaces of the substrates (Figure 5 a-c), but no coverage of nanoparticles was achieved in the internal part of the substrate (Figure 5 d-f), suggesting that no PDA coating was present in the internal pores. Consequently, the depth of penetration and diffusion of the dopamine solution is the limiting factor in determining the functionalization of the internal areas in the presence of porous scaffolds. Considering the scaffold used in the study, a homogenous, efficient coating was achieved over at least 0.6 cm of depth within the scaffolds. Further analysis (Figure 6) showed that the penetration could be, potentially, much larger. The porosities on the external area presented good AgNP coverage (Figure 6a,b), while in the central area of the scaffold (Figure 6e,f) the absence of PDA prevented the nucleation of nanoparticles, as observed previously. In the mid-range area, the coverage was not homogenous, between different pores (Figure 6c,d) as well as within the same pore. Figure 5Sd shows the inhomogeneous coverage of nanoparticles on subsequent 3D-printed layers in the same pore. Penetration depth has been proposed to be dependent on various parameters, such as the pore size, the dopamine concentration in solution, the deposition time, as well as the presence of agitation during the dopamine polymerization and deposition<sup>48</sup>, or the elimination of the nitrogen drying in between the two steps, to avoid the formation of air bubbles inside the scaffold.

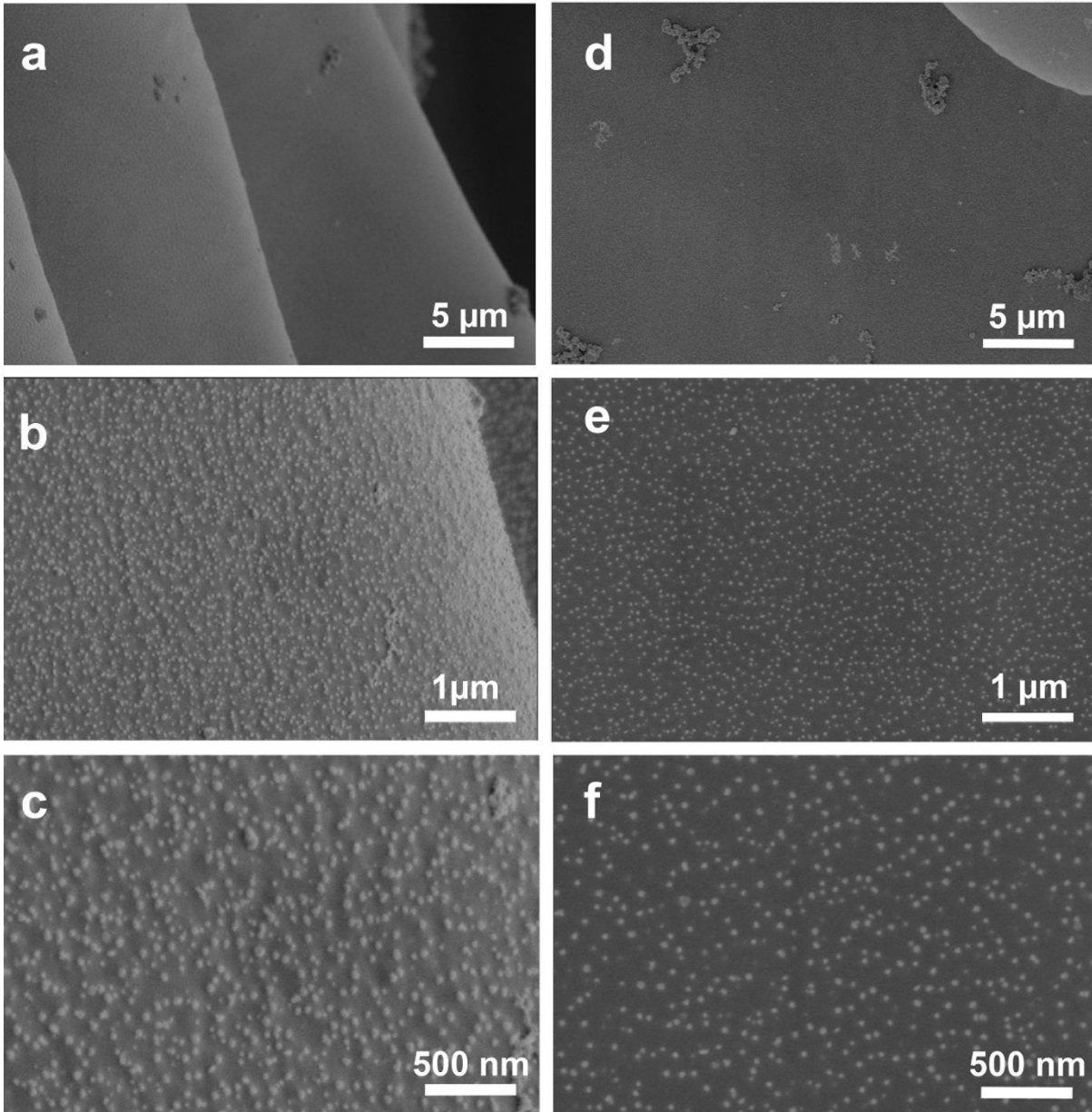
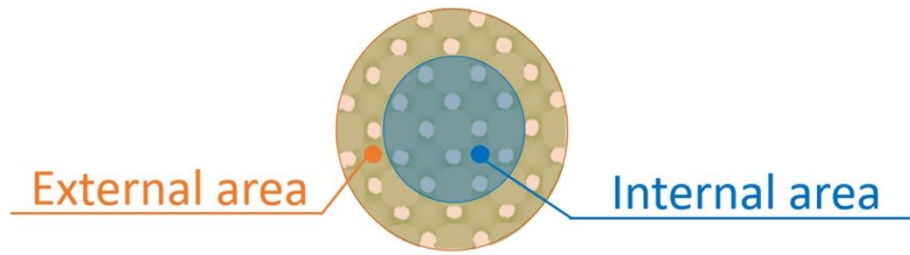


Figure 4. SEM micrographs of a porous resin sample functionalized with PDA coating and coated with carbon tape on the bottom and top circular surfaces before the immersion in silver nitrate solution. Images show the nanoparticle coverage inside a pore on the external area (a-c) and internal area (d-f) of the substrate at progressive magnifications (10k, 50k, 100k).

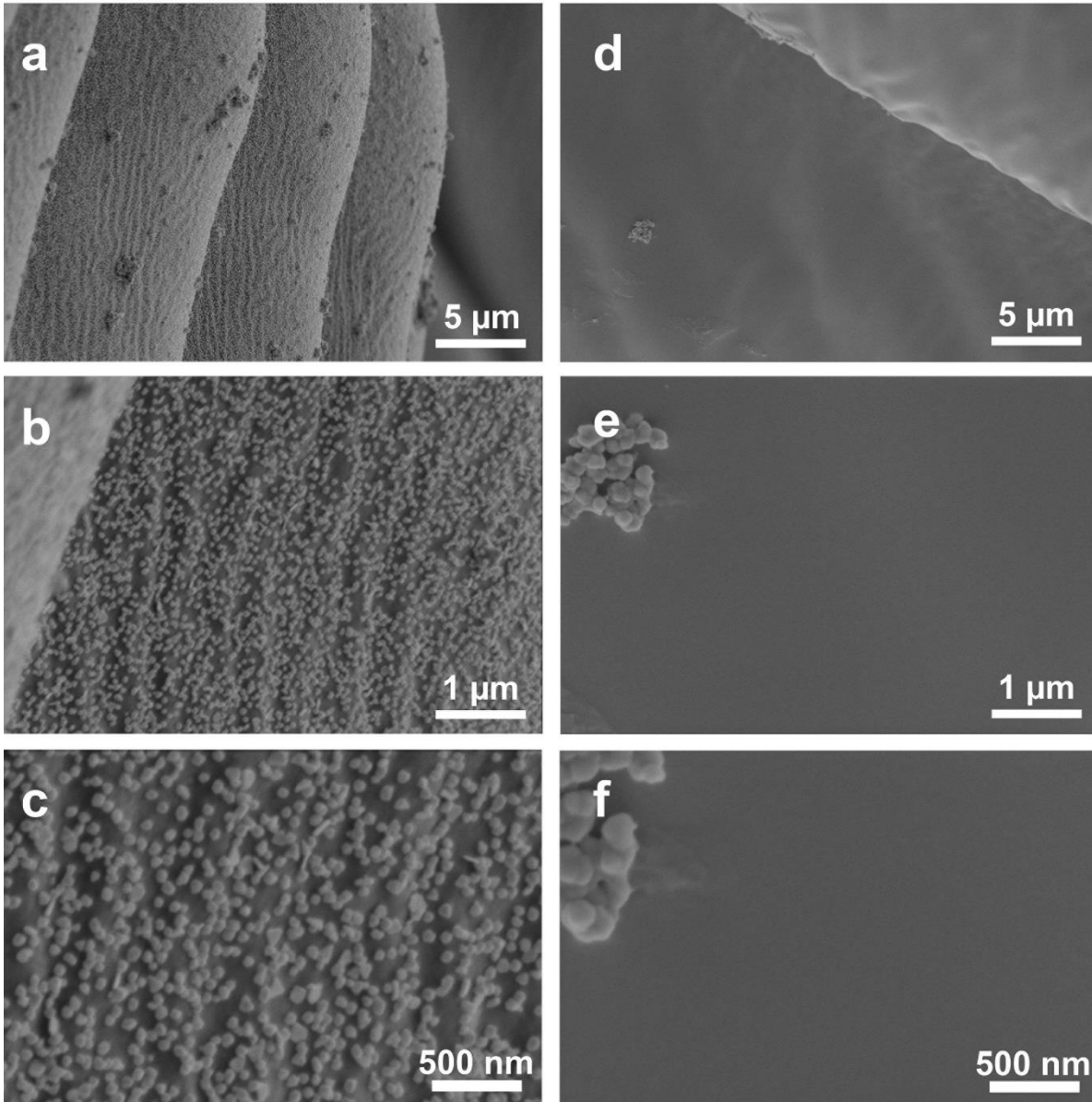
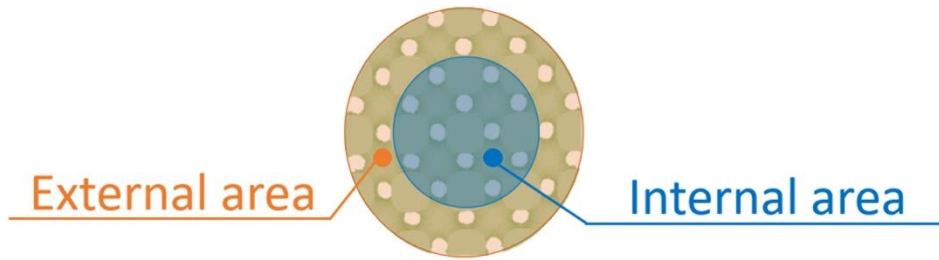


Figure 5. Scanning electron micrographs of a porous resin sample coated with carbon tape on the bottom and top circular surfaces before the PDA coating step and subsequent nanoparticle deposition. Images in the figure show the nanoparticle coverage inside a pore on the external area (a-c) and internal area (d-f) of the substrate at progressive magnifications (10k, 50k, 100k). The internal area of the scaffold does not show PDA coating, nor does it present immobilized nanoparticles. The residue in the image is probably due to contamination and debris of the polymer resin.

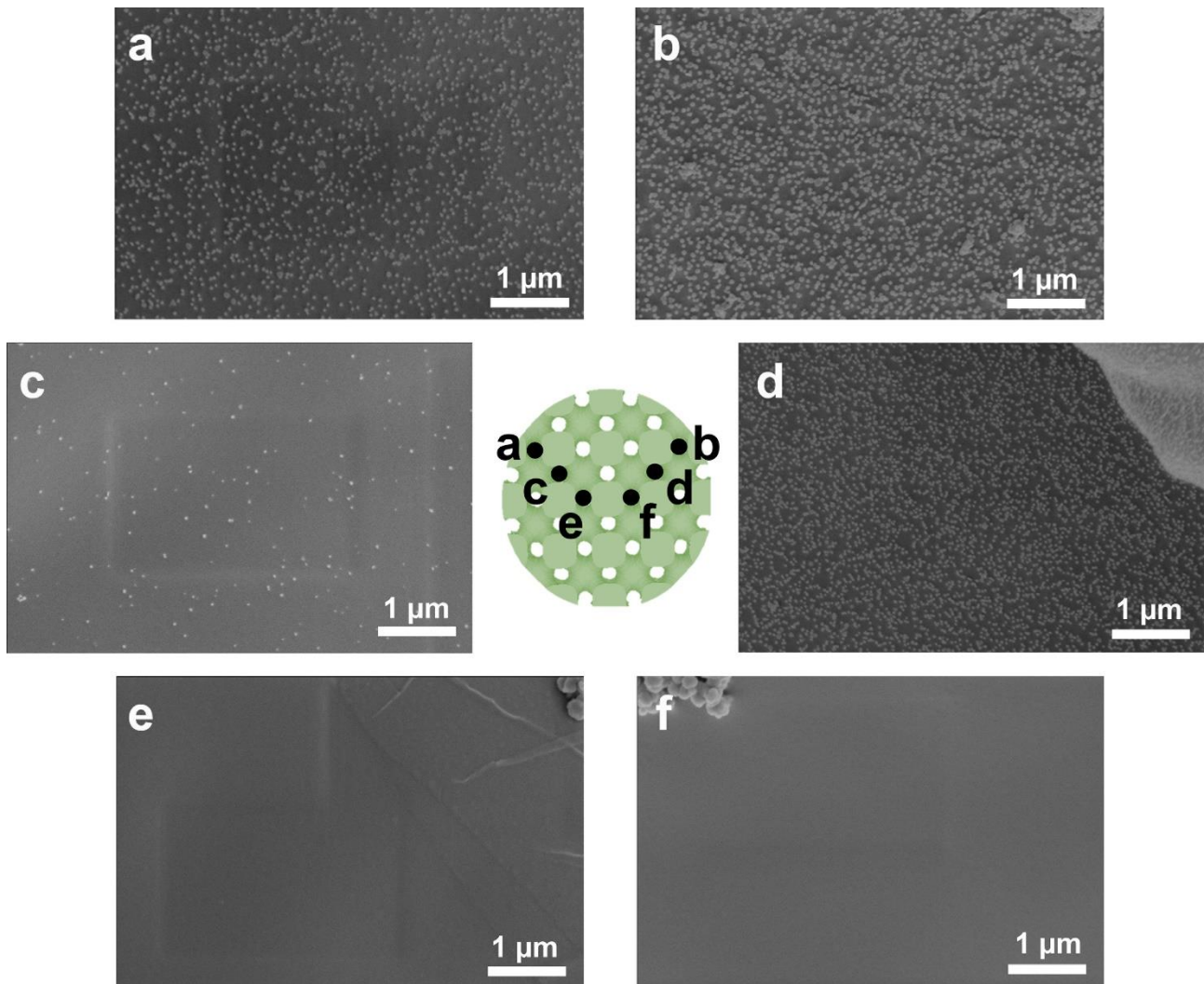


Figure 6. Scanning electron micrographs of a porous resin sample coated with carbon tape on the bottom and top circular surfaces after the PDA coating step but before the subsequent AgNP deposition. Images in the figure show the nanoparticle coverage inside a pore on the external area (a-b), middle area (c-d) and internal area (e-f) of the substrate along two specular radial directions at a magnification of 50k. The internal area of the scaffold does not show PDA coating, nor does it present immobilized nanoparticles. The coverage of the middle area is inhomogeneous and possibly dependent on phenomena that hinder the normal perfusion of the scaffold, like the presence of air bubbles.

Silver nanoparticles convey their antibacterial function through different mechanisms, that seem to be complementary more than alternative to each other, and are dependent on nanoparticle size and possible functionalization<sup>49–52</sup>. In particular, silver nanoparticles can alter the bacterial membrane structure and integrity, cause damage to the DNA by inducing the formation of reactive oxygen species, or progressively dissolve to release silver ions. Such silver ions can bind to thiol-groups contained in membrane proteins in the cell and, in turn, inhibit their growth and functions. Analysis of the cytotoxicity of the substrates for bone-interfacing applications was pursued through the culturing of the osteosarcoma Saos-2 cell line, whose proliferation was assessed through an AlamarBlue assay at three different time points: days 1, 4 and 7. For this purpose, the preparation of the substrates for mammalian culture followed the steps described in Section 3.3 of the Materials and Methods. Results and their significance are presented in Figure 7. The control group consisted of a tissue culture polystyrene surface at the bottom of 24-well plates. For all substrates, cell proliferation was significantly increased from day 1 to day 7, and no statistical significance was found between the control and the samples at the last time point, confirming that the AgNPs did not induce cytotoxic effects toward the Saos-2 cells for this nanoparticle size and concentration, in agreement with previous results<sup>53</sup>.

In addition, both the solid and porous substrates coated with PDA and with nucleated AgNPs showed significant growth after 4 days of culture with respect to the first time point. Overall, our results suggest that both porosity and the presence of sub-micron topographical cues favor earlier cell proliferation and favor

preliminary osteointegration processes<sup>37,38</sup>. Contrarily to previous studies<sup>54-56</sup>, the PDA coating alone did not enhance cell proliferation, suggesting that specific responses to PDA could be cell line-dependent or dependent on the underlying topography of the PDA coating.

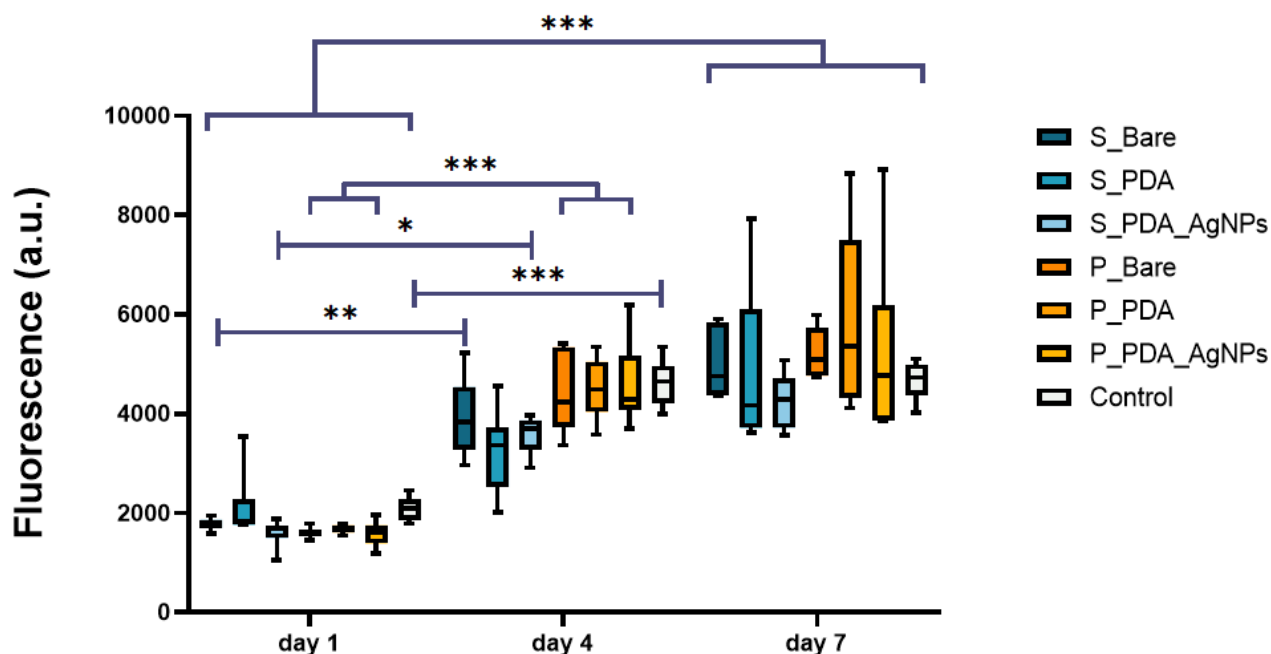


Figure 7. Saos-2 cell metabolism on bare, PDA-coated and PDA+AgNPs coated substrates. None of the substrates presented cytotoxicity over 7 days of culture when compared with the control. Porous (P) scaffolds, regardless of coating, showed significantly higher proliferation after 4 days compared to solid (S) components, as well as solid and porous substrates with PDA coating and AgNPs. \* indicates  $p < 0.05$ , \*\* for  $p < 0.005$ , \*\*\* for  $p < 0.0005$ ,  $n = 3$ .

Bacterial infections are significant roadblocks to implant success and their occurrence often necessitates removal of the implant. *S. aureus* is a pathogen that is responsible for a majority of implant infections, and the increased prevalence of its drug-resistant forms are of great concern<sup>57,58</sup>. The use of implants resistant to bacterial colonization would mitigate chances of infection.

The resistance to bacterial colonization of the different substrates was assessed both in the planktonic state and through analysis of biofilm formation. For both analysis, the preparation of the substrates for bacterial culture followed the steps described in Section 3.3 of the Materials and Methods. The concentration of the *S. aureus* biofilm in terms of CFU/mL on the different substrates after 24 hours of incubation is shown in Figure 8a. Results showed that coating with PDA and subsequent deposition of AgNPs resulted in significantly less biofilm formation on both the solid and porous resin, with reductions of approximately 3.9 log and 3.5 log, respectively, as compared to the uncoated samples, whereas no statistically significant difference was observed for the substrates without AgNPs. The biofilm formation on the samples coated only with PDA was not statistically different than that of the uncoated samples for both solid and porous substrates. In conclusion, the results demonstrated that the AgNPs coating significantly decreased *S. aureus* biofilm formation on both the solid and porous resin after 24 hours of incubation at human body temperature. Interestingly, porous samples were expected to support a higher degree of biofilm formation due to the increased surface area, however, differences in biofilm concentration between respective solid and porous samples were not found to be statistically significant on a logarithmic scale.

The variation in optical density of the bacterial suspensions, which correlates to bacterial concentration, after 24 hours of incubation with the different substrates was measured (Figure 8b). OD of the surrounding bacterial suspension was not significantly different for the uncoated or PDA coated substrates as compared

to a bacterial control. This suggests that the substrates themselves and the PDA coating have no effect on the surrounding suspension. However, the *S. aureus* suspensions incubated with the AgNPs coated substrates exhibited a significantly lower OD, confirming that the antimicrobial properties of the coating derive from the metal deposition.

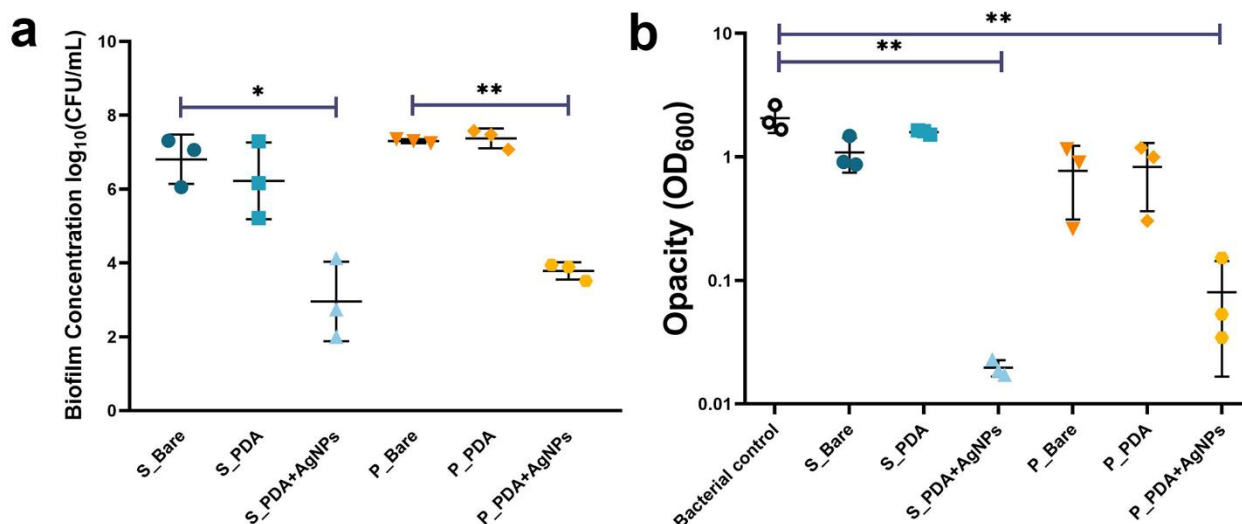


Figure 8. a) Concentration of *S. aureus* Newman biofilm on the substrates after 24 hours of incubation at 37 °C. Results are plotted as individual biological replicates, where each biological replicate is an average of two technical replicates, and the horizontal line represents the mean for each set of samples. There is no significant difference in biofilm concentration between the bare substrates and the PDA-coated substrates for both the solid (S) and the porous (P) samples. Samples coated with PDA + AgNPs showed significantly less biofilm formation than the uncoated or PDA-coated control samples. b) Optical density of a *S. aureus* Newman suspension after 24 hours of 37 °C incubation with different sample coatings. Opacity of the bacterial suspension, which correlates with concentration, was significantly lower when exposed to the substrates coated with PDA + AgNPs as compared to the samples without AgNPs. \* stands for  $p < 0.05$ , \*\* for  $p < 0.005$ .

Different from previously reported results<sup>59–61</sup>, no inherent antibacterial activity was found for PDA-coated samples, either for the planktonic state or for biofilm formation, suggesting that the PDA layer does not necessarily hold any intrinsic antibacterial activity. It has been hypothesized that the bactericidal characteristics of such coatings are connected to their surface roughness<sup>48</sup>, which in turn is correlated to the preparation method: static incubation with dopamine hydrochloride solutions, like the one used in this research, generally results in more homogenous coatings with no antibacterial activity, while incubation under dynamic stirring can lead to increased surface roughness that results in contact-active antibacterial activity<sup>48</sup>.

The difference in performance between the bactericidal effect in planktonic state and the biofilm inhibition suggests that the antibacterial mechanisms of silver nanoparticles may include contact-induced bacterial death, a hindering of replication mechanism, or a combination of the two<sup>62</sup>. Further investigation is needed for a comprehensive understanding of the mechanisms participating in the antimicrobial activity of the silver nanoparticles.

Regardless of the precise mechanisms in action, numerous works suggest that an effective concentration of silver nanoparticles in solution to reach the Minimum Inhibitory Concentration (MIC) on *S. aureus* can be found in the range of ten to a thousand  $\mu\text{g/mL}$ <sup>63–65</sup>. Different values reported are based on differences in size, shape, and surface functionality of the nanoparticles, deriving from the synthesis method used to produce them<sup>66</sup>. For silver nanoparticles with sizes similar to those obtained in this work, a value around 180  $\mu\text{g/mL}$  seems to be an effective MIC<sup>67</sup>. In this work, in contrast to other techniques to synthesize silver nanoparticles, the reducing agent used to form the nanoparticles is the polydopamine layer that coats the scaffold surface. The nucleated nanoparticles are therefore always immobilized on the surface, and not free-floating in a colloidal suspension like in most other works that address the effect of silver nanoparticles on

bacteria. As such, the direct comparison with results deriving from colloidal suspensions of nanoparticles may be only partially representative.

It is known that the silver ions released in solutions play an important role in the antibacterial activity of AgNPs. The outcomes of ICP-OES on the leachate after 24 hours of incubation at 37 °C indicated a release of ~5% of the total silver originally deposited in the form of nanoparticles, with a different concentration in solution between solid ( $0.78 \pm 0.08$  ppm) and porous substrates ( $1.0 \pm 0.1$  ppm), likely due to the difference in surface area available for the coating. The calibration curve for ICP-OES and correlated data is shown in Figure S6 of the Supporting Information.

Compared to the effective inhibitory concentration observed for silver ions toward the same bacterial strain<sup>68</sup>, found to be of 20 ppm, the concentration of silver ions detected during the ICP-OES (~ppm), is sufficient to promote inhibition.

Silver nanoparticles and ions have also been reported to exhibit cyto- and genotoxicity toward mammalian cells<sup>29-31</sup>. To probe the viability of the mammalian cells when exposed to silver ions leached by the substrates, a Live/Dead kit was used on Saos-2 cells cultured in media supplemented with silver-ions to evaluate cell viability. Image analysis conducted on the pictures captured from the confocal microscope, three for each concentration, for which an example is provided in Figure S7, suggests that while the presence of silver ions in solution does result in some viability loss with respect to the control, the retained viability at the ionic concentration detected through ICP-OES (1 ppm) is high enough for the substrate to be defined as non-cytotoxic according to the ISO standard 10993-5. The observed viability for control, 0.1 ppm Ag<sup>+</sup> supplemented media, 1 ppm Ag<sup>+</sup> supplemented media and 10 ppm Ag<sup>+</sup> supplemented media were 95±1%, 86 ±1%, 75±2% and 58±4%, respectively. According to ISO 10993-5, only the highest concentration of silver ions in solution exhibited mild cytotoxicity, causing around 50% decrease in normal cell functionality. Furthermore, while the release of silver ions, in reality, would follow a continuous increase in the curve profile during the 24 hours, in this case the addition of silver ions to the culture media in specific concentrations was applied upon cell seeding.

As a proof-of-concept, solid titanium disks were coated in two steps following the same procedure used for the polymeric substrates (Figure 9). Electron microscopy micrograph analysis indicated a smaller particle area and nanoparticle diameter with respect to the polymer substrate ( $1820 \pm 280$  nm<sup>2</sup> and  $48 \pm 4$  nm, respectively) but similar surface coverage of nanoparticles, equal to  $19.3 \pm 0.6$  %. A histogram showing the distribution of the nanoparticle sizes on the titanium substrate is presented in Figure S3e.

The discrepancy with respect to the polymeric substrates is possibly associated with the different surface density of specific moieties exposed by the PDA after the formation of the coating layer, which could affect the number of nucleation sites, and in turn the number and size of nanoparticles generated on the coating layer. Nonetheless, the results on titanium attest to the transferability of the coating method as-is to other substrates with different surface chemistry and particular clinical relevance. In addition, PDA can serve for the nucleation of other metals, like copper<sup>14,24,25</sup> or platinum<sup>69,70</sup>, thus further expanding the host of applications for the method under investigation, even outside of the biomedical sector.

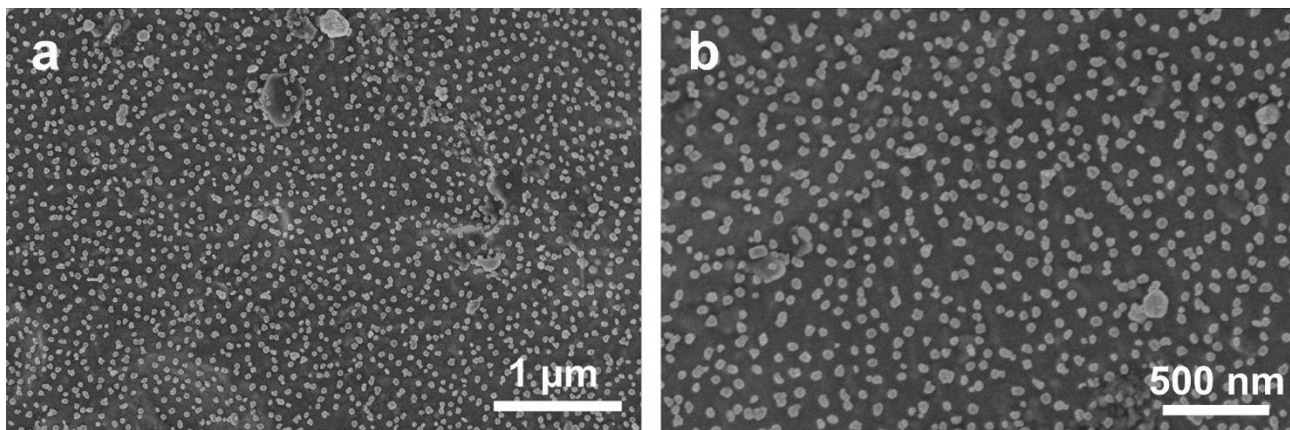


Figure 9. Overview (a) and magnified (b) scanning electron micrographs showing the surface coverage of a titanium substrate functionalized with PDA coating and subsequent AgNP nucleation.

## 5. Conclusions

The contamination of scaffold surfaces for bone-interfacing applications can result in complications for the patient and the necessity of revision surgeries, given the limited efficacy of antibiotics on bacterial biofilms. The present investigation demonstrates an effective two-stage functionalization method for scaffolds using a PDA coating and AgNPs formation. After the first coating step to deposit a PDA layer on the surface, AgNPs are nucleated from solution to convey antibacterial properties. The implementation of porous geometries and the presence of the PDA-AgNPs surface coating both encouraged earlier osteoblast-like cell proliferation, while reducing bacteria in the planktonic state and decreasing the formation of a biofilm. The antimicrobial activity could be related to the leaching of silver ions into solution, as shown by ICP-OES, during sustained contact with fluids, which hinders the normal functionalities of bacterial cells. Overall, the total amount of silver ions leached was at a concentration in the range of parts per million, even lower than the concentrations used in previous works that reported the ability to reduce bacterial proliferation, and below the range of cytotoxicity toward osteoblastic cells.

The choice of PDA as the first step in the functionalization, on which the nanoparticle deposition is dependent, makes the technique easily transferable to different substrate materials, and paves the way for other applications. As shown through the proof-of-concept with titanium, slight differences may be present in the nanoparticle size and coverage, which in turn may alter the cellular and bacterial response. Definitive conclusions on the cytotoxicity and antibacterial efficacy of such coating will require in-vivo studies. The depth of penetration of the functionalization, around 0.6 cm in the current study, could possibly be improved by favoring the perfusion of the dopamine solution through shaking. Finally, the coating is intended for the coverage of static areas of prosthetics; therefore, for use in areas that undergo tribological phenomena, mechanical and abrasion tests would be required to address the host response to any debris. In conclusion, while further investigations are warranted, the noteworthy bactericidal characteristics displayed by the coating under investigation and its scalability demonstrate a promising method to decrease the risk of biofilm formation following surgeries and prevent the necessity of revisions.

## Supporting Information

Infographic on coating method, additional qualitative assessment of nanoparticles coverage on substrate, coating penetration, tape test, and ICP-OES results.

## Acknowledgments

Microscopy was carried out at the Canadian Center for Electron Microscopy at McMaster University. In vitro studies were performed at the Biointerfaces Institute at McMaster University. K.G., J.M.-M., and K.N.S. acknowledge funding support from NSERC (grants RGPIN-2020-05722, RGPIN-2019-06433, and RGPIN-2022-05258, respectively), K.G. and J.M.-M. acknowledge support from the Ontario Ministry of Research,

Innovation, and Science (Early Researcher Awards), and the Canada Research Chairs Program (K.G. holds the Tier II Chair in Microscopy of Biomaterials and Biointerfaces, and J.M-M. holds the Tier II Chair in Micro- and Nanostructured Materials). A.M. acknowledges the support of the Foundation Blanceflor Boncompagni Ludovisi, née Bildt and Mitacs (Application Ref. IT27778). BioRender was used for schematics and the graphical abstract.

## Credit Author Statement

**Alessandra Merlo**: investigation, methodology, formal analysis, writing - original draft, visualization. **Eduardo Gonzalez-Martinez**: investigation, methodology, writing - original draft. **Kamal Saad**: investigation, methodology, writing - original draft. **Mellissa Gomez**: investigation, methodology, formal analysis, writing - original draft. **Manjot Grewal**: investigation, formal analysis, writing - original draft. **Joseph Deering**: investigation, methodology, formal analysis, writing - original draft. **Liza-Anastasia Di Cecco**: investigation, writing - original draft. **Zeinab Hosseinidou**: supervision, funding. **Kyla Sask**: supervision, funding. **Jose Moran-Mirabal**: conceptualization, supervision, funding. **Kathryn Grandfield**: conceptualization, supervision, funding. All authors wrote, reviewed and edited the present manuscript.

## References

- (1) Raphel, J.; Holodniy, M.; Goodman, S. B.; Heilshorn, S. C. Multifunctional Coatings to Simultaneously Promote Osseointegration and Prevent Infection of Orthopaedic Implants. *Biomaterials* **2016**, *84*, 301–314. <https://doi.org/10.1016/j.biomaterials.2016.01.016>.
- (2) Donlan, R. M. Biofilm Formation: A Clinically Relevant Microbiological Process. *Clin. Infect. Dis.* **2001**, *33* (8), 1387–1392. <https://doi.org/10.1086/322972>.
- (3) Salkind, A. R.; Rao, K. C. Antibiotic Prophylaxis to Prevent Surgical Site Infections. *Am. Fam. Physician* **2011**, *83* (5), 585–590.
- (4) Høiby, N.; Bjarnsholt, T.; Givskov, M.; Molin, S.; Ciofu, O. Antibiotic Resistance of Bacterial Biofilms. *Int. J. Antimicrob. Agents* **2010**, *35* (4), 322–332. <https://doi.org/10.1016/j.ijantimicag.2009.12.011>.
- (5) Stewart, P. S. Mechanisms of Antibiotic Resistance in Bacterial Biofilms. *Int. J. Med. Microbiol.* **2002**, *292* (2), 107–113. <https://doi.org/10.1078/1438-4221-00196>.
- (6) Renner, L. D.; Weibel, D. B. Physicochemical Regulation of Biofilm Formation. *MRS Bull.* **2011**, *36* (5), 347–355. <https://doi.org/10.1557/mrs.2011.65>.
- (7) Bjarnsholt, T.; Buhlin, K.; Dufrière, Y. F.; Gomelsky, M.; Moroni, A.; Ramstedt, M.; Rumbaugh, K. P.; Schulte, T.; Sun, L.; Åkerlund, B.; Römling, U. Biofilm Formation – What We Can Learn from Recent Developments. *J. Intern. Med.* **2018**, *284* (4), 332–345. <https://doi.org/10.1111/joim.12782>.
- (8) Ryu, J. H.; Messersmith, P. B.; Lee, H. Polydopamine Surface Chemistry: A Decade of Discovery. *ACS Appl. Mater. Interfaces* **2018**, *10* (9), 7523–7540. <https://doi.org/10.1021/acsami.7b19865>.
- (9) GhavamiNejad, A.; Aguilar, L. E.; Ambade, R. B.; Lee, S. H.; Park, C. H.; Kim, C. S. Immobilization of Silver Nanoparticles on Electropolymerized Polydopamine Films for Metal Implant Applications. *Colloids Interface Sci. Commun.* **2015**, *6*, 5–8. <https://doi.org/10.1016/j.colcom.2015.08.001>.
- (10) Yu, X.; Walsh, J.; Wei, M. Covalent Immobilization of Collagen on Titanium through Polydopamine Coating to Improve Cellular Performances of MC3T3-E1 Cells. *RSC Adv.* **2014**, *4* (14), 7185–7192. <https://doi.org/10.1039/c3ra44137g>.
- (11) Black, K. C. L.; Yi, J.; Rivera, J. G.; Zelasko-Leon, D. C.; Messersmith, P. B. Polydopamine-Enabled Surface Functionalization of Gold Nanorods for Cancer Cell-Targeted Imaging and Photothermal Therapy. *Nanomedicine* **2013**, *8* (1), 17–28. <https://doi.org/10.2217/nnm.12.82>.
- (12) Hu, Y.; Dan, W.; Xiong, S.; Kang, Y.; Dhinakar, A.; Wu, J.; Gu, Z. Development of Collagen/Polydopamine Complexed Matrix as Mechanically Enhanced and Highly Biocompatible

Semi-Natural Tissue Engineering Scaffold. *Acta Biomater.* **2017**, *47*, 135–148.  
<https://doi.org/10.1016/j.actbio.2016.10.017>.

- (13) Jeong, Y. K.; Park, S. H.; Choi, J. W. Mussel-Inspired Coating and Adhesion for Rechargeable Batteries: A Review. *ACS Appl. Mater. Interfaces* **2018**, *10*, 7562–7573.  
<https://doi.org/10.1021/acsami.7b08495>.
- (14) Gonzalez-Martinez, E.; Saem, S. (Kevin); Beganovic, N. E.; Moran-Mirabal, J. Fabrication of Microstructured Electrodes via Electroless Metal Deposition onto Polydopamine-coated Polystyrene Substrates and Thermal Shrinking. *Nano Sel.* **2021**, *2* (10), 1926–1940.  
<https://doi.org/10.1002/nano.202100022>.
- (15) Chen, C.; Sun, W.; Lv, H.; Li, H.; Wang, Y.; Wang, P. Spacer Arm-Facilitated Tethering of Laccase on Magnetic Polydopamine Nanoparticles for Efficient Biocatalytic Water Treatment. *Chem. Eng. J.* **2018**, *350* (130), 949–959. <https://doi.org/10.1016/j.cej.2018.06.008>.
- (16) Kim, S.; Gim, T.; Jeong, Y.; Ryu, J. H.; Kang, S. M. Facile Construction of Robust Multilayered PEG Films on Polydopamine-Coated Solid Substrates for Marine Antifouling Applications. *ACS Appl. Mater. Interfaces* **2018**, *10*, 7626–7631. <https://doi.org/10.1021/acsami.7b07199>.
- (17) Liu, M.; Zeng, G.; Wang, K.; Wan, Q.; Tao, L.; Zhang, X.; Wei, Y. Recent Developments in Polydopamine: An Emerging Soft Matter for Surface Modification and Biomedical Applications. *Nanoscale* **2016**, *8* (38), 16819–16840. <https://doi.org/10.1039/c5nr09078d>.
- (18) Ball, V. Polydopamine Films and Particles with Catalytic Activity. *Catal. Today* **2018**, *301*, 196–203. <https://doi.org/10.1016/j.cattod.2017.01.031>.
- (19) Schanze, K. S.; Lee, H.; Messersmith, P. B. Ten Years of Polydopamine: Current Status and Future Directions. *ACS Appl. Mater. Interfaces* **2018**, *10* (9), 7521–7522.  
<https://doi.org/10.1021/acsami.8b02929>.
- (20) Ball, V.; Frari, D. Del; Toniazzo, V.; Ruch, D. Kinetics of Polydopamine Film Deposition as a Function of PH and Dopamine Concentration: Insights in the Polydopamine Deposition Mechanism. *J. Colloid Interface Sci.* **2012**, *386* (1), 366–372. <https://doi.org/10.1016/j.jcis.2012.07.030>.
- (21) Shin, Y. M.; Lee, Y. Bin; Shin, H. Time-Dependent Mussel-Inspired Functionalization of Poly(l-Lactide-Co-ε-Caprolactone) Substrates for Tunable Cell Behaviors. *Colloids Surfaces B Biointerfaces* **2011**, *87* (1), 79–87. <https://doi.org/10.1016/j.colsurfb.2011.05.004>.
- (22) Malollari, K. G.; Delparastan, P.; Sobek, C.; Vachhani, S. J.; Fink, T. D.; Zha, R. H.; Messersmith, P. B. Mechanical Enhancement of Bioinspired Polydopamine Nanocoatings. *ACS Appl. Mater. Interfaces* **2019**, *11* (46), 43599–43607. <https://doi.org/10.1021/acsami.9b15740>.
- (23) Zhou, P.; Deng, Y.; Lyu, B.; Zhang, R.; Zhang, H.; Ma, H.; Lyu, Y.; Wei, S. Rapidly-Deposited Polydopamine Coating via High Temperature and Vigorous Stirring: Formation, Characterization and Biofunctional Evaluation. *PLoS One* **2014**, *9* (11), e113087.  
<https://doi.org/10.1371/journal.pone.0113087>.
- (24) Yang, J.; Xu, H.; Zhang, L.; Zhong, Y.; Sui, X.; Mao, Z. Lasting Superhydrophobicity and Antibacterial Activity of Cu Nanoparticles Immobilized on the Surface of Dopamine Modified Cotton Fabrics. *Surf. Coatings Technol.* **2017**, *309*, 149–154. <https://doi.org/10.1016/j.surfcoat.2016.11.058>.
- (25) Duan, X.; Liu, S.; Huang, E.; Shen, X.; Wang, Z.; Li, S.; Jin, C. Superhydrophobic and Antibacterial Wood Enabled by Polydopamine-Assisted Decoration of Copper Nanoparticles. *Colloids Surfaces A Physicochem. Eng. Asp.* **2020**, *602* (June), 125145. <https://doi.org/10.1016/j.colsurfa.2020.125145>.
- (26) Ye, W.; Wang, D.; Zhang, H.; Zhou, F.; Liu, W. Electrochemical Growth of Flowerlike Gold Nanoparticles on Polydopamine Modified ITO Glass for SERS Application. *Electrochim. Acta* **2010**, *55*

(6), 2004–2009. <https://doi.org/10.1016/j.electacta.2009.11.022>.

- (27) Kailasa, S. K.; Park, T.-J.; Rohit, J. V.; Koduru, J. R. Antimicrobial Activity of Silver Nanoparticles. In *Nanoparticles in Pharmacotherapy*; Elsevier, 2019; pp 461–484. <https://doi.org/10.1016/B978-0-12-816504-1.00009-0>.
- (28) Rai, M.; Yadav, A.; Gade, A. Silver Nanoparticles as a New Generation of Antimicrobials. *Biotechnol. Adv.* **2009**, *27* (1), 76–83. <https://doi.org/10.1016/j.biotechadv.2008.09.002>.
- (29) Park, M. V. D. Z.; Neigh, A. M.; Vermeulen, J. P.; De, L. J. J.; Verharen, H. W.; Briedé, J. J.; Loveren, H. Van; Jong, W. H. De. The Effect of Particle Size on the Cytotoxicity, in Flammation, Developmental Toxicity and Genotoxicity of Silver Nanoparticles. *Biomaterials* **2011**, *32* (36), 9810–9817. <https://doi.org/10.1016/j.biomaterials.2011.08.085>.
- (30) Guo, X.; Li, Y.; Yan, J.; Ingle, T.; Jones, M. Y.; Boudreau, M. D.; Cunningham, C. K.; Abbas, M.; Angel, M.; Zhou, T.; Moore, M. M.; Howard, P. C.; Chen, T.; Guo, X.; Li, Y.; Yan, J.; Ingle, T.; Jones, M. Y.; Boudreau, M. D.; Cunningham, C. K.; Abbas, M.; Paredes, A. M.; Zhou, T.; Moore, M. M.; Howard, P. C.; Size-, T. C.; Guo, X.; Li, Y.; Yan, J.; Ingle, T.; Jones, M. Y.; Mei, N.; Boudreau, M. D. Size- and Coating-Dependent Cytotoxicity and Genotoxicity of Silver Nanoparticles Evaluated Using in Vitro Standard Assays Size- and Coating-Dependent Cytotoxicity and Genotoxicity of Silver. *Nanotoxicology* **2016**, *10* (9), 1373–1384. <https://doi.org/10.1080/17435390.2016.1214764>.
- (31) Kim, T.; Kim, M.; Park, H.; Shin, U. S.; Gong, M.; Kim, H. Size-Dependent Cellular Toxicity of Silver Nanoparticles. *J. Biomed. Mater. Res. A* **2012**, *100A* (4), 1033–1043. <https://doi.org/10.1002/jbm.a.34053>.
- (32) Shi, W. L. X. Q.; Chen, Y. Antibacterial Effect of Silver Nanoparticles on Staphylococcus Aureus. *Biometals* **2011**, *24*, 135–141. <https://doi.org/10.1007/s10534-010-9381-6>.
- (33) Gupta, S.; Claonadh, N. O.; Casey, A.; Chambers, G. Comparative in Vitro Cytotoxicity Study of Silver Nanoparticle on Two Mammalian Cell Lines. *Toxicol. Vitr.* **2012**, *26* (2), 238–251. <https://doi.org/10.1016/j.tiv.2011.12.004>.
- (34) Abbasi, N.; Hamlet, S.; Love, R. M.; Nguyen, N. T. Porous Scaffolds for Bone Regeneration. *J. Sci. Adv. Mater. Devices* **2020**, *5* (1), 1–9. <https://doi.org/10.1016/j.jsamd.2020.01.007>.
- (35) Hernandez, J. L.; Woodrow, K. A. Medical Applications of Porous Biomaterials : Features of Porosity and Tissue-Specific Implications for Biocompatibility. *Adv. Healthc. Mater.* **2022**, *11*, 2102087. <https://doi.org/10.1002/adhm.202102087>.
- (36) Lewallen, E. A.; Riester, S. M.; Bonin, C. A.; Kremers, H. M.; Dudakovic, A.; Kakar, S.; Cohen, R. C. Biological Strategies for Improved Osseointegration and Osteoinduction of Porous Metal Orthopedic Implants. **2015**, *21* (2), 218–230. <https://doi.org/10.1089/ten.teb.2014.0333>.
- (37) Karageorgiou, V.; Ā, D. K. Porosity of 3D Biomaterial Scaffolds and Osteogenesis. *Biomaterials* **2005**, *26*, 5474–5491. <https://doi.org/10.1016/j.biomaterials.2005.02.002>.
- (38) Deering, J.; Grandfield, K. Current Interpretations on the in Vivo Response of Bone to Additively Manufactured Metallic Porous Scaffolds : A Review. *Biomater. Biosyst.* **2021**, *2* (February), 100013. <https://doi.org/10.1016/j.bbiosy.2021.100013>.
- (39) Schneider, C. A.; Rasband, W. S.; Eliceiri, K. W. NIH Image to ImageJ: 25 Years of Image Analysis. *Nat. Methods* **2012**, *9* (7), 671–675. <https://doi.org/10.1038/nmeth.2089>.
- (40) Deering, J.; Clifford, A.; D’Elia, A.; Zhitomirsky, I.; Grandfield, K. Composite Dip Coating Improves Biocompatibility of Porous Metallic Scaffolds. *Mater. Lett.* **2020**, *274*, 128057. <https://doi.org/10.1016/j.matlet.2020.128057>.
- (41) Baba, T.; Bae, T.; Schneewind, O.; Takeuchi, F.; Hiramatsu, K. Genome Sequence of Staphylococcus

Aureus Strain Newman and Comparative Analysis of Staphylococcal Genomes : Polymorphism and Evolution of Two Major Pathogenicity Islands. *J. Bacteriol.* **2008**, *190* (1), 300–310. <https://doi.org/10.1128/JB.01000-07>.

- (42) Kucharíková, S.; Gerits, E.; De Brucker, K.; Braem, A.; Ceh, K.; Majdič, G.; Španič, T.; Pogorevc, E.; Verstraeten, N.; Tournu, H.; Delattin, N.; Impellizzeri, F.; Erdtmann, M.; Krona, A.; Lövenklev, M.; Knezevic, M.; Fröhlich, M.; Vleugels, J.; Fauvart, M.; De Silva, W. J.; Vandamme, K.; Garcia-Forgas, J.; Cammue, B. P. A.; Michiels, J.; Van Dijck, P.; Thevissen, K. Covalent Immobilization of Antimicrobial Agents on Titanium Prevents Staphylococcus Aureus and Candida Albicans Colonization and Biofilm Formation. *Journal of Antimicrobial Chemotherapy*. 2016, pp 936–945. <https://doi.org/10.1093/jac/dkv437>.
- (43) Greenspan, L. Humidity Fixed Points of Binary Saturated Aqueous Solutions. *J. Res. Natl. Bur. Stand. Sect. A Phys. Chem.* **1977**, *81A* (1), 89. <https://doi.org/10.6028/jres.081A.011>.
- (44) Hidalgo, E.; Domínguez, C. Study of Cytotoxicity Mechanisms of Silver Nitrate in Human Dermal Fibroblasts. *Toxicol. Lett.* **1998**, *98* (3), 169–179. [https://doi.org/10.1016/S0378-4274\(98\)00114-3](https://doi.org/10.1016/S0378-4274(98)00114-3).
- (45) Lu, Z.; Xiao, J.; Wang, Y.; Meng, M. In Situ Synthesis of Silver Nanoparticles Uniformly Distributed on Polydopamine-Coated Silk Fibers for Antibacterial Application. *J. Colloid Interface Sci.* **2015**, *452*, 8–14. <https://doi.org/10.1016/j.jcis.2015.04.015>.
- (46) Davies, J. E.; Ajami, E.; Moineddin, R.; Mendes, V. C. The Roles of Different Scale Ranges of Surface Implant Topography on the Stability of the Bone/Implant Interface. *Biomaterials* **2013**, *34* (14), 3535–3546. <https://doi.org/10.1016/j.biomaterials.2013.01.024>.
- (47) Brånemark, R.; Emanuelsson, L.; Palmquist, A.; Thomsen, P. Bone Response to Laser-Induced Micro- and Nano-Size Titanium Surface Features. *Nanomedicine Nanotechnology, Biol. Med.* **2011**, *7* (2), 220–227. <https://doi.org/10.1016/j.nano.2010.10.006>.
- (48) Su, L.; Yu, Y.; Zhao, Y.; Liang, F.; Zhang, X. Strong Antibacterial Polydopamine Coatings Prepared by a Shaking-Assisted Method. *Sci. Rep.* **2016**, *6* (March), 1–8. <https://doi.org/10.1038/srep24420>.
- (49) Yin, I. X.; Zhang, J.; Zhao, I. S.; Mei, M. L.; Li, Q.; Chu, C. H. The Antibacterial Mechanism of Silver Nanoparticles and Its Application in Dentistry. *Int. J. Nanomedicine* **2020**, *15*, 2555–2562. <https://doi.org/10.2147/IJN.S246764>.
- (50) Qing, Y.; Cheng, L.; Li, R.; Liu, G.; Zhang, Y.; Tang, X.; Wang, J.; Liu, H.; Qin, Y. Potential Antibacterial Mechanism of Silver Nanoparticles and the Optimization of Orthopedic Implants by Advanced Modification Technologies. *Int. J. Nanomedicine* **2018**, *13*, 3311–3327. <https://doi.org/10.2147/IJN.S165125>.
- (51) Le Ouay, B.; Stellacci, F. Antibacterial Activity of Silver Nanoparticles: A Surface Science Insight. *Nano Today* **2015**, *10* (3), 339–354. <https://doi.org/10.1016/j.nantod.2015.04.002>.
- (52) Durán, N.; Durán, M.; de Jesus, M. B.; Seabra, A. B.; Fávaro, W. J.; Nakazato, G. Silver Nanoparticles: A New View on Mechanistic Aspects on Antimicrobial Activity. *Nanomedicine Nanotechnology, Biol. Med.* **2016**, *12* (3), 789–799. <https://doi.org/10.1016/j.nano.2015.11.016>.
- (53) Michalakis, K.; Bakopoulou, A.; Papachristou, E.; Vasilaki, D.; Tsouknidas, A.; Michailidis, N.; Johnstone, E. Evaluation of the Response of HOS and Saos-2 Osteosarcoma Cell Lines When Exposed to Different Sizes and Concentrations of Silver Nanoparticles. *Biomed Res. Int.* **2021**. <https://doi.org/10.1155/2021/5013065>.
- (54) Tsai, W. B.; Chen, W. T.; Chien, H. W.; Kuo, W. H.; Wang, M. J. Poly(Dopamine) Coating to Biodegradable Polymers for Bone Tissue Engineering. *J. Biomater. Appl.* **2014**, *28* (6), 837–848. <https://doi.org/10.1177/0885328213483842>.

- (55) Luo, R.; Tang, L.; Zhong, S.; Yang, Z.; Wang, J.; Weng, Y.; Tu, Q.; Jiang, C.; Huang, N. In Vitro Investigation of Enhanced Hemocompatibility and Endothelial Cell Proliferation Associated with Quinone-Rich Polydopamine Coating. *ACS Appl. Mater. Interfaces* **2013**, *5* (5), 1704–1714. <https://doi.org/10.1021/am3027635>.
- (56) Aysin, F.; Yilmaz, A.; Yilmaz, M. Metallic Nanoparticle-Decorated Polydopamine Thin Films and Their Cell Proliferation Characteristics. *Coatings* **2020**, *10* (9), 802. <https://doi.org/10.3390/coatings10090802>.
- (57) Montanaro, L.; Testoni, F.; Poggi, A.; Visai, L.; Speziale, P.; Arciola, C. R. Emerging Pathogenetic Mechanisms of the Implantrelated Osteomyelitis by Staphylococcus Aureus. *Int. J. Artif. Organs* **2011**, *34* (9), 781–788. <https://doi.org/10.5301/ijao.5000052>.
- (58) Oliveira, W. F.; Silva, P. M. S.; Silva, R. C. S.; Silva, G. M. M.; Machado, G.; Coelho, L. C. B. B.; Correia, M. T. S. Staphylococcus Aureus and Staphylococcus Epidermidis Infections on Implants. *J. Hosp. Infect.* **2018**, *98* (2), 111–117. <https://doi.org/10.1016/j.jhin.2017.11.008>.
- (59) Karkhanechi, H.; Takagi, R.; Matsuyama, H. Biofouling Resistance of Reverse Osmosis Membrane Modified with Polydopamine. *Desalination* **2014**, *336* (1), 87–96. <https://doi.org/10.1016/j.desal.2013.12.033>.
- (60) He, X.; Obeng, E.; Sun, X.; Kwon, N.; Shen, J.; Yoon, J. Polydopamine, Harness of the Antibacterial Potentials-A Review. *Mater. Today Bio* **2022**, *15* (May), 100329. <https://doi.org/10.1016/j.mtbio.2022.100329>.
- (61) Fu, Y.; Yang, L.; Zhang, J.; Hu, J.; Duan, G.; Liu, X.; Li, Y.; Gu, Z. Polydopamine Antibacterial Materials. *Mater. Horizons* **2021**, *8* (6), 1618–1633. <https://doi.org/10.1039/d0mh01985b>.
- (62) Siddiqi, K. S.; Husen, A.; Rao, R. A. K. A Review on Biosynthesis of Silver Nanoparticles and Their Biocidal Properties. *J. Nanobiotechnology* **2018**, *16* (1). <https://doi.org/10.1186/s12951-018-0334-5>.
- (63) Parvekar, P.; Palaskar, J.; Metgud, S.; Maria, R.; Dutta, S. The Minimum Inhibitory Concentration (MIC) and Minimum Bactericidal Concentration (MBC) of Silver Nanoparticles against Staphylococcus Aureus. *Biomater. Investig. Dent.* **2020**, *7* (1), 105–109. <https://doi.org/10.1080/26415275.2020.1796674>.
- (64) Wang, H.; Wang, M.; Xu, X.; Gao, P.; Xu, Z.; Zhang, Q.; Li, H.; Yan, A.; Kao, R. Y. T.; Sun, H. Multi-Target Mode of Action of Silver against Staphylococcus Aureus Endows It with Capability to Combat Antibiotic Resistance. *Nat. Commun.* **2021**, *12* (1). <https://doi.org/10.1038/s41467-021-23659-y>.
- (65) Bruna, T.; Maldonado-Bravo, F.; Jara, P.; Caro, N. Silver Nanoparticles and Their Antibacterial Applications. *Int. J. Mol. Sci.* **2021**, *22* (13). <https://doi.org/10.3390/ijms22137202>.
- (66) Swolana, D.; Wojtyczka, R. D. Activity of Silver Nanoparticles against Staphylococcus Spp. *Int. J. Mol. Sci.* **2022**, *23* (8). <https://doi.org/10.3390/ijms23084298>.
- (67) Agnihotri, S.; Mukherji, S.; Mukherji, S. Size-Controlled Silver Nanoparticles Synthesized over the Range 5-100 Nm Using the Same Protocol and Their Antibacterial Efficacy. *RSC Adv.* **2014**, *4* (8), 3974–3983. <https://doi.org/10.1039/c3ra44507k>.
- (68) Li, H.; You, Q.; Feng, X.; Zheng, C.; Zeng, X.; Xu, H. Effective Treatment of Staphylococcus Aureus Infection with Silver Nanoparticles and Silver Ions. *J. Drug Deliv. Sci. Technol.* **2023**, *80* (January), 104165. <https://doi.org/10.1016/j.jddst.2023.104165>.
- (69) Wang, W.; Wang, Z.; Sun, M.; Zhang, H.; Wang, H. Ligand-Free Sub-5 Nm Platinum Nanocatalysts on Polydopamine Supports: Size-Controlled Synthesis and Size-Dictated Reaction Pathway Selection. *Nanoscale* **2022**, *14*, 5743–5750. <https://doi.org/10.1039/d2nr00805j>.
- (70) Yu, X.; Wang, H.; Guo, L.; Wang, L. Self-Assembled Platinum Nanoflowers on Polydopamine-Coated

Reduced Graphene Oxide for Methanol Oxidation and Oxygen Reduction Reactions. **2014**, 3221–3227. <https://doi.org/10.1002/asia.201402883>.